

Structure tensor based automated detection of macular edema and central serous retinopathy using optical coherence tomography images

BILAL HASSAN,^{1,*} GULISTAN RAJA,¹ TAIMUR HASSAN,² AND M. USMAN AKRAM³

¹Faculty of Electronics and Electrical Engineering, University of Engineering and Technology, Taxila 47050, Pakistan

²Department of Electrical Engineering, Bahria University, Islamabad 44000, Pakistan

³Department of Computer Engineering, National University of Sciences and Technology, Islamabad, Pakistan

*Corresponding author: bilz@live.com

Received 19 November 2015; revised 17 January 2016; accepted 23 January 2016; posted 25 January 2016 (Doc. ID 254162); published 4 March 2016

Macular edema (ME) and central serous retinopathy (CSR) are two macular diseases that affect the central vision of a person if they are left untreated. Optical coherence tomography (OCT) imaging is the latest eye examination technique that shows a cross-sectional region of the retinal layers and that can be used to detect many retinal disorders in an early stage. Many researchers have done clinical studies on ME and CSR and reported significant findings in macular OCT scans. However, this paper proposes an automated method for the classification of ME and CSR from OCT images using a support vector machine (SVM) classifier. Five distinct features (three based on the thickness profiles of the sub-retinal layers and two based on cyst fluids within the sub-retinal layers) are extracted from 30 labeled images (10 ME, 10 CSR, and 10 healthy), and SVM is trained on these. We applied our proposed algorithm on 90 time-domain OCT (TD-OCT) images (30 ME, 30 CSR, 30 healthy) of 73 patients. Our algorithm correctly classified 88 out of 90 subjects with accuracy, sensitivity, and specificity of 97.77%, 100%, and 93.33%, respectively. © 2016 Optical Society of America

OCIS codes: (110.4500) Optical coherence tomography; (100.2960) Image analysis; (100.0100) Image processing; (170.4470) Ophthalmology; (100.5010) Pattern recognition.

<http://dx.doi.org/10.1364/JOSAA.33.000455>

1. INTRODUCTION

The macula is an oval-shaped, highly pigmented dark spot at the center of the retinal layer. It has a diameter of approximately a quarter of an inch. The macula is responsible for the central vision. Central vision is important for daily routine tasks such as reading, driving, and writing. Near the center of the macula is a tiny dip packed with light-sensitive cells called fovea. The fovea pick up the finest details of central vision. Macular disorders mainly damage the macular region of the retina, and can greatly affect the central vision of a person. Unfortunately, in developing countries such as Pakistan, the population ratio of visually impaired people is increasing day by day due to the lack of basic health infrastructure [1]. Globally, the major cause of blindness is cataracts, followed by macular disorders [2]. There are many types of macular disorders, but some common ones are macular edema (ME), central serous retinopathy (CSR), macular hole (MH), age-related macular degeneration (AMD), and the Förster–Fuchs retinal spot. Most of these macular disorders are curable if diagnosed at an early stage, but due to negligence and lack of awareness, over 2 million people in Pakistan are

completely blind. Therefore, there is a dire need to create an awareness of these diseases among the people and to facilitate ophthalmologists with accurate and efficient detection methods.

In the case of ME, the retinal layers are swollen due to the leakage of fluid from retinal blood vessels. There are two major causes of ME. The first one is diabetes, where small blood capillaries within the retina start leaking fluid. In this case, ME is termed diabetic macular edema (DME). Eye (cataract) surgery may also increase the risk of developing macular edema due to irritated blood vessels and fluid leakage. In this case, ME is termed cystoid macular edema (CME). CSR occurs due to the accumulation of serous fluid beneath the retina and causes the retinal layers to detach. There are two types of CSR. In Type 1 CSR, the fluid accumulates under the neurosensory retina [3]. Type II is characterized by the accumulation of fluid in the retina due to retinal pigment epithelium (RPE) leakage [3]. Serous fluid in such cases tends to be shallower rather than domed shaped. Common symptoms of ME and CSR are dim, blurred, and distorted central vision [4,5].



Fig. 1. (a) Healthy person vision. (b) ME- and CSR-affected vision.

Figure 1 shows the vision of a healthy person and a person with ME/CSR.

Multiple retinal testing techniques are in practice nowadays, including ophthalmoscopy, fundus photography, and fundus fluorescein angiography. In addition to these, optical coherence tomography (OCT) imaging is also being used for testing retinal-disorder subjects. The OCT imaging technique works on the principle of the Michelson-type interferometer in which a beam splitter is used to split a low-coherence beam into two waves. One beam is directed toward the subject's eye and the other toward the reference mirror, which is placed equidistant. These waves are reflected back and are recombined to produce an axial scan (A-scan), which is detected by the detector [6]. The foremost advantage that OCT imaging technology has over other existing techniques is that symptoms of retinal diseases such as CSR, ME, and pigment epithelial detachments (PEDs) appear in the early stages in OCT images [7]. In the case of an OCT scan that shows signs of ME and CSR, the increased thickness between the inner limiting membrane (ILM) and the choroid can be observed due to the fluid accumulation between both layers, as shown in Fig. 2.

In the past, many researchers have done clinical studies on ME and CSR using OCT images. Hannouche and Ávila [8] did a comparison between various eye testing techniques. They observed fundography, bio-microscopy, fluorescein angiography (FA), and OCT imaging techniques for the detection of diabetic foveal edema and concluded that OCT imaging is more sensitive to retinal changes than the rest of the techniques. Shrestha *et al.* [9] figured out how the OCT imaging technique can be more useful in aligning the macula after surgery in the case of ME. They studied 60 subjects and concluded that OCT is very effective in evaluating ME. Zhang *et al.* [10] presented an overview of OCT imaging technology and how it can be used in the treatment of DME. Ferrara *et al.* [11] characterized features of the RPE layer and choroid of CSR-affected patients. They included 15 eyes of 13 patients and concluded that the OCT imaging technique enables the characterization of pathologic features of the RPE layer and choroid in patients with CSR. Wani *et al.* [12] used OCT imaging and FA for the

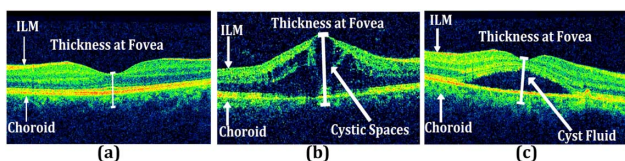


Fig. 2. OCT scan. (a) Healthy person OCT scan. (b) ME-affected OCT scan. (c) CSR-affected OCT scan.

diagnosis of CSR [12]. They studied 48 CSR-affected eyes and concluded that OCT can be used as complementary tool for the diagnosis of CSR. Teke *et al.* [13] discussed the comparison of fundus auto fluorescence (FAF) and OCT imaging for CSR-affected patients. They evaluated 100 CSR cases and concluded that both FAF and OCT imaging techniques can support the clinicians in evaluating and diagnosing CSR [13].

Some researchers also worked on automated detection of ME and PEDs using OCT images. Zhang *et al.* [14] did a coarse segmentation of the intra-retinal layers for detection of CME. They used AdaBoost in their research and obtained an accuracy of 98.6%. Wilkins *et al.* [15] detected the fluid between retinal layers by manually identifying the ILM and RPE layer. They applied their algorithm to 16 patients and obtained an average sensitivity of 91% and an average specificity of 96%. Sugruk *et al.* [16] proposed a method for the detection of AMD and DME. They removed the retinal nerve fiber layer for RPE detection, and from the RPE abnormality, they detected AMD. They also detected cysts bubbles for the detection of DME. They obtained accuracies of 86.6% for DME and 100% for AMD. Sahar *et al.* [17] segmented the ILM and choroid layer for the detection of DME and in healthy subjects using the software development life cycle (SDLC) algorithm. They achieved an accuracy, sensitivity, and specificity of 84%, 93%, and 80%, respectively. Srinivasan *et al.* [18] classified AMD, DME, and healthy OCT images using histogram-oriented descriptors as a feature vector that is computed from an input B-scan. After that, the feature vector was passed to an SVM for automated classification. Their accuracy for AMD, DME, and healthy scans was 100%, 100%, and 86.67%, respectively. Lee *et al.* [19] used spatial domain OCT (SD-OCT) scans of 46 eyes with AMD and CSR to automatically classify PEDs into three categories: serous, drusenoid, or fibrovascular. They used the mean internal intensity and the standard deviation of the internal intensity to categorize PEDs and achieved an overall accuracy of 89.2%. Cabrera Fernández *et al.* [20,21] used a structure tensor approach combined with a nonlinear diffusion process for automated detection of the retinal layers. However, this paper proposes an automated method for the classification of macular edema and central serous retinopathy using OCT scans. The remainder of the paper is organized as follows: Section 2 explains the proposed methodology, while the results are discussed in Section 3. Section 4 concludes the paper.

2. PROPOSED METHODOLOGY

We proposed an automated algorithm for the classification of three retinal pathologies, as shown in Fig. 3. For correct classification, it is important to de-noise and enhance the input OCT scan ($I_{RGB}(x, y)$), which is done in the preprocessing stage. After that, the ILM and choroid are segmented using highly coherent two-dimensional (2D) structure tensors. To obtain the tensors, we computed the dot product of the partial derivatives of the images at 0 deg and 90 deg [22]. In addition to this, the proposed algorithm automatically detects cyst fluid segments that are present between inter-retinal layers. The thickness vector ($Tn(y)$) is computed between the ILM and choroid by measuring an absolute difference between both layers for each A-scan. At last, a five-dimensional (5D) feature

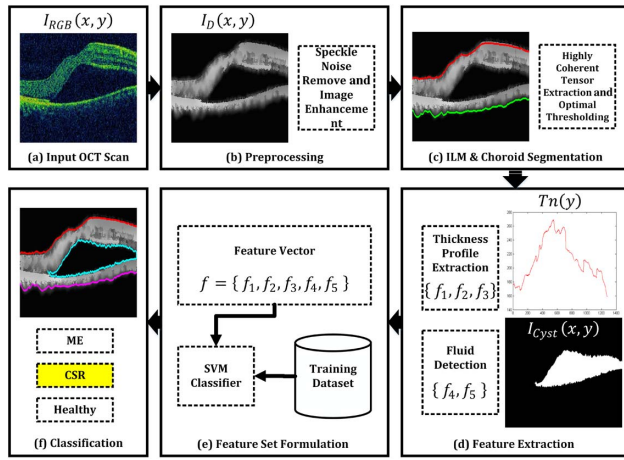


Fig. 3. Proposed system. (a) Candidate OCT scan. (b) Preprocessing stage to obtain de-noised image ($I_D(x, y)$). (c) ILM (red) and choroid (green) layers segmentation using highly coherent 2D structure tensors. (d) Thickness vector ($Tn(y)$) computation and three features (f_1, f_2, f_3) extraction from it, and cyst fluid detection and two features (f_4, f_5) extraction from it. (e) Feature vector passed to SVM for classification. (f) Classification stage based on feature vector and training datasets.

set based on the thickness vector and cyst fluid is obtained. The feature set is then passed to a supervised SVM classifier to classify the retinal OCT scans.

A. OCT Dataset

We acquired an OCT dataset from the Armed Forces Institute of Ophthalmology (AFIO) in Rawalpindi. It consists of 90 time domain OCT (TD-OCT) scans of 73 patients, out of which 54 were male and 19 were female. The median age of the patients is 36.2 years. As shown in Table 1, 56 patients had unilateral while 17 patients had bilateral disease. The total number of eyes was 90 (30 healthy, 30 CSR, and 30 ME). The range of the scanning parameters of all three retinal subjects is shown in Table 1.

B. Preprocessing

The preprocessing stage is intended to improve the quality of the OCT scan. First of all, an input OCT scan ($I_{RGB}(x, y)$) is resized to a common resolution of 480×1280 using MATLAB's

Table 1. Scanning Parameters of Dataset

Scanning Parameters	Type		
	Healthy	CSR	ME
Total subjects	30	30	30
Axial resolution (μm)	3–3.8	3–3.8	3–3.8
Lateral resolution (μm)	11–13	7–13	11–13
Azimuthal resolution (μm)	49–122	58–129	63–186
Scan Resolution (pixel x pixel)	480×1280	480×1280	480×1280
B-scans	128	115–134	117–126
A-scans (points)	1280	1280	1280
	points	points	points

built-in command *imresize*. Next, it is converted into a grayscale OCT scan ($I_{GRAY}(x, y)$). After that, different image enhancement techniques, including contrast adjustment, image filtering, and morphological operations, are carried out. The proposed system also uses a 2D adaptive low-pass Wiener filter, which estimates the local mean and variance within the neighborhood of each pixel $I_D(x_i, y_j)$ of the candidate image as expressed in Eqs. (1)–(3):

$$\mu = \frac{1}{\omega_x \omega_y} \sum_{x_i \in \omega_x} \sum_{y_j \in \omega_y} I(x_i, y_j), \quad (1)$$

$$\sigma^2 = \frac{1}{\omega_x \omega_y} \sum_{x_i \in \omega_x} \sum_{y_j \in \omega_y} I^2(x_i, y_j) - \mu^2, \quad (2)$$

$$I_D(x_i, y_j) = \mu + \frac{\sigma^2 - v^2}{\sigma^2} (I(x_i, y_j) - \mu), \quad (3)$$

where $I_D(x_i, y_j)$ is the de-noised pixel, ω_x are the row-wise kernel pixels, ω_y are the column-wise kernel pixels, μ is the local estimated mean, σ^2 is the local estimated variance, and v^2 is the average of all local estimated variances [23]. After enhancement, the de-noised OCT image $I_D(x, y)$ is converted into a binary image $I_B(x, y)$ for further processing, as shown in Fig. 4.

C. ILM and Choroid Segmentation

To accurately segment the ILM and choroid layers from the de-noised OCT scan $I_D(x, y)$, we obtained 2D structure tensors by taking the dot product of the partial derivatives of the images at 0 deg and 90 deg with a Gaussian window $\text{win}(x, y)$. In the past, some researchers also used the same approach for the segmentation of the sub-retinal layers. Cabrera Fernández *et al.* [20,21] used a structure tensor approach combined with a non-linear diffusion process for the automated detection of the retinal layers. A structure tensor is a second-moment matrix that shows the similarities and prominent orientations of image gradients within the pixel neighborhood. The 2D discrete structure tensor is illustrated by Eqs. (4)–(7):

$$J_w(x, y) = \begin{bmatrix} (I_X(x, y))^2 & I_X(x, y)I_Y(x, y) \\ I_Y(x, y)I_X(x, y) & (I_Y(x, y))^2 \end{bmatrix}, \quad (4)$$

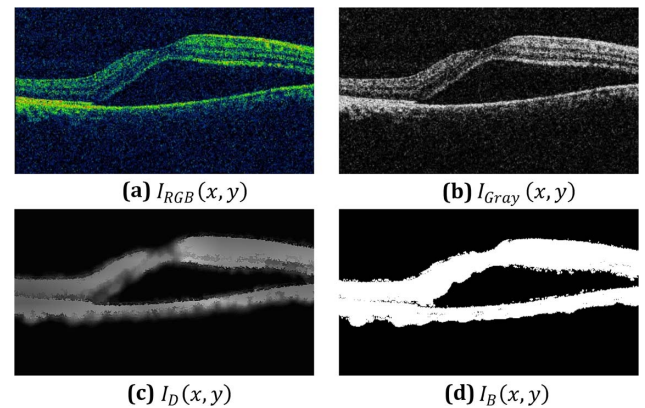


Fig. 4. Preprocessing stage. (a) Input OCT scan ($I_{RGB}(x, y)$). (b) Grayscale OCT scan ($I_{GRAY}(x, y)$). (c) De-noised image ($I_D(x, y)$). (d) Binary image ($I_B(x, y)$).

$$(I_X(x, y))^2 = \sum_{x_i \in w_x} \sum_{y_j \in w_y} \text{win}(x_i, y_j) I_{\rho X}, \quad (5)$$

$$\begin{aligned} I_X(x, y) I_Y(x, y) &= I_Y(x, y) I_X(x, y) \\ &= \sum_{x_i \in w_x} \sum_{y_j \in w_y} \text{win}(x_i, y_j) I_{\rho XY}, \end{aligned} \quad (6)$$

$$(I_Y(x, y))^2 = \sum_{x_i \in w_x} \sum_{y_j \in w_y} \text{win}(x_i, y_j) I_{\rho Y}, \quad (7)$$

where $J_w(x, y)$ is a structure tensor matrix of dimensions 2×2 . $(I_X(x, y))^2$ is the horizontally oriented tensor, $(I_X(x, y) I_Y(x, y))$ and $(I_Y(x, y) I_X(x, y))$ are horizontally and vertically oriented tensors, and $(I_Y(x, y))^2$ is the vertically oriented tensor, modeled using the radiative transfer equation or its diffusion approximation [24]. $I_{\rho Y}$, $I_{\rho XY}$, and $I_{\rho X}$ are the partial derivatives of the de-noised image within the pixel neighborhood as expressed by Eqs. (8)–(10). $\text{win}(x, y)$ is the Gaussian window, and $I_D(x, y)$ is the de-noised OCT scan. These four tensors are shown in Fig. 5:

$$I_{\rho Y} = \left(\frac{\partial I_D(x - x_i, y - y_j)}{\partial y} \right)^2, \quad (8)$$

$$I_{\rho XY} = \left(\frac{\partial I_D(x - x_i, y - y_j)}{\partial x} \right) \left(\frac{\partial I_D(x - x_i, y - y_j)}{\partial y} \right), \quad (9)$$

$$I_{\rho X} = \left(\frac{\partial I_D(x - x_i, y - y_j)}{\partial x} \right)^2. \quad (10)$$

The relative difference between the two eigenvalues indicates the degree of anisotropy of the gradient in the Gaussian window $\text{win}(x, y)$. This quantity is termed the “coherence” and is expressed by Eq. (11):

$$C_w = \left(\frac{\lambda_1 - \lambda_2}{\lambda_1 + \lambda_2} \right). \quad (11)$$

where “ λ_1 ” and “ λ_2 ” are the eigenvalues for the horizontal and vertical orientations within $\text{win}(x, y)$, respectively. The value of coherence (C_w) determines the orientation alignment within the window. $C_w = 1$ corresponds to the maximally aligned

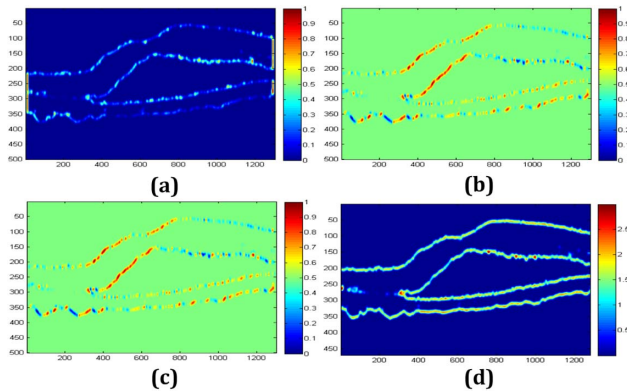


Fig. 5. 2D structure tensors of $I_D(x, y)$: (a) horizontally oriented gradients tensor ($(I_X(x, y))^2$). (b), (c) Vertically and horizontally oriented gradients tensors, and (d) vertically oriented gradients tensor ($(I_Y(x, y))^2$).

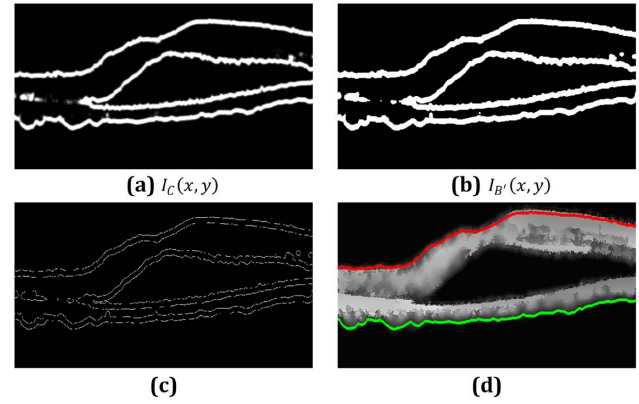


Fig. 6. ILM and choroid layer segmentation: (a) highly coherent tensor ($I_C(x, y)$). (b) Binary map $I_{B'}(x, y)$ of highly coherent tensor. (c) Canny edge detection of sub-retinal and choroid layers. (d) Segmented ILM (red) and choroid (green) layer.

orientation ($C_w = -1$ indicates alignment in the opposite direction), and if $C_w = 0$, then there is no predominant orientation [24].

Out of these four tensors, a highly coherent tensor $I_C(x, y)$ is extracted, and is then converted into a binary coherent tensor $I_{B'}(x, y)$ by finding the optimal threshold using the Otsu algorithm [25]. At last, from $I_{B'}(x, y)$, the ILM and choroid are segmented using canny edge detection [26], as shown in Fig. 6.

D. Features Extraction

From the segmented ILM and choroid, we extracted a thickness profile by computing the absolute difference between both layers. We have also detected the cyst fluid between the sub-retinal layers using these segmented layers.

1. Thickness Profile Extraction

After segmenting the sub-retinal pathology from $I_{B'}(x, y)$, the thickness vector $Tn(y)$ is computed from the ILM and choroid by measuring the absolute difference between both layers for each A-scan as illustrated by Eqs. (12) and (13):

$$Tn(y) = [Tn(y_1), Tn(y_2), \dots, Tn(y_i)], \quad (12)$$

where

$$Tn(y_i) = (|I_{ILM_i}(x, y) - I_{Choro_{s_i}}(x, y)|). \quad (13)$$

“ i ” is the number of A-scans present in one B-scan. Figure 7 shows the B-scan of a CSR-affected case, and Fig. 8 shows the thickness profile plot of respective B-scan.

2. Cyst Fluid Detection

Along with extracting the B-scan thickness profile, we have also detected the cyst segments within the sub-retinal pathology. After extracting the ILM and choroid from the coherent tensor, a sub-retinal mask $I_{Mask}(x, y)$ is created between both layers. Figure 9 shows the cyst segment extracted by performing an exclusive OR (XOR) operation between the sub-retinal mask and de-noised binary image as expressed in Eq. (14):

$$I_{Cyst}(x, y) = I_{Mask}(x, y) \oplus I_B(x, y). \quad (14)$$

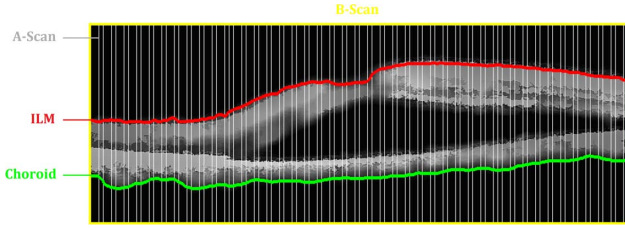


Fig. 7. B-scan of CSR-affected subject with A-scan after every 10 A-scans. ILM (red) and choroid (green) layers depicted on de-noised image ($I_D(x, y)$).

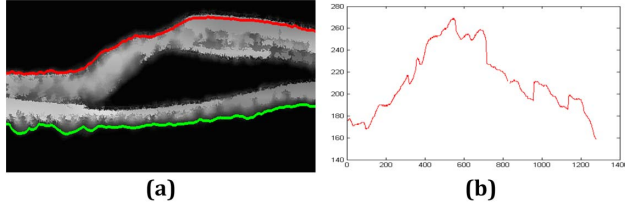


Fig. 8. (a) Segmented ILM and choroid layers. (b) Thickness plot between ILM and choroid layers.

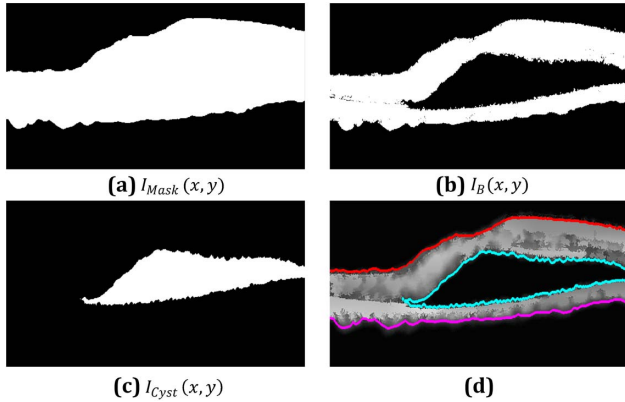


Fig. 9. Cyst fluid detection: (a) mask between ILM and choroid layer ($I_{Mask}(x, y)$). (b) Binary de-noised image ($I_B(x, y)$). (c) XORed image of (a) and (b). (d) Cyst fluid mapped on $I_D(x, y)$.

In order to distinguish between ME and CSR subjects, the proposed method computes the one-level wavelet decomposition of the cyst thickness profile, as shown in Fig. 10. Then, the cyst energy from the low band is calculated to discriminate between the ME and CSR cases. The value of this cyst energy is much less in case of CSR subjects as compared to ME subjects, as shown in Fig. 11.

E. Feature Set Formulation

To automatically distinguish between healthy, ME, and CSR OCT scans, we extracted five distinct features from all retinal images to form the feature vector ($f = \{f_1, f_2, f_3, f_4, f_5\}$). Three features are obtained from the thickness profiles of the ILM and choroid, and two are obtained from the cyst fluid present within the sub-retinal layers. The explanation of each

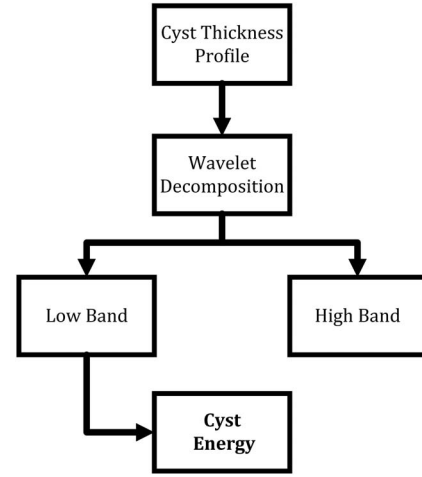


Fig. 10. One-level wavelet decomposition to calculate cyst energy.

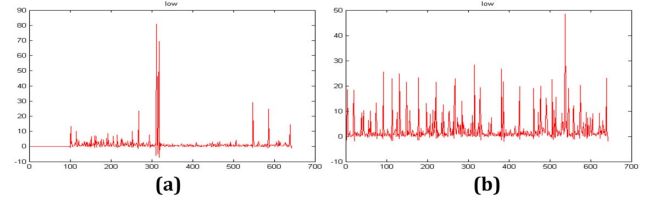


Fig. 11. Cyst energy: (a) CSR case and (b) ME case.

feature to distinguish between all three retinal pathologies is as follows:

Max Thickness (f_1): The maximum value in the thickness vector $Tn(y)$, which is due to the maximum gap between the ILM and choroid, as expressed by Eqs. (15) and (16):

$$f_1 = \max[Tn(y)], \quad (15)$$

$$f_1 = \max[|I_{ILM}(x, y) - I_{Choroid}(x, y)|]. \quad (16)$$

Min Thickness (f_2): The minimum value in the thickness vector $Tn(y)$, which is due to the minimum gap between the ILM and choroid layer, as expressed by Eqs. (17) and (18):

$$f_2 = \min[Tn(y)], \quad (17)$$

$$f_2 = \min[|I_{ILM}(x, y) - I_{Choroid}(x, y)|]. \quad (18)$$

Thickness Variation (f_3): The difference between f_2 and f_1 as expressed by Eq. (19). It tells about the variation between the layers due to the presence of cyst fluid between the sub-retinal layers:

$$f_3 = f_2 - f_1. \quad (19)$$

Maximum Cyst Area (f_4): The maximum cyst area determines the total area occupied by the leaked fluid within sub-retinal layers. It is computed by taking the area of $I_{Cyst}(x, y)$, as expressed by Eq. (20):

$$f_4 = \text{Area}(I_{Cyst}(x, y)). \quad (20)$$

Cyst Energy (f_5): The total energy of a cyst segment calculated by Eq. (21):

Table 2. Range of Features Extracted

Type	Cases	Features				
		F1 (mm)	F2 (mm)	F3 (mm)	F4 (mm ²)	F5
Healthy	Case 1	36.51	11.38	25.14	124.27	1165.2
	Case 2	39.69	23.02	16.67	140.28	1328.8
	Case 3	34.13	19.58	14.55	0	0
	Case 4	50.54	32.54	17.99	126.71	1124.1
	Case 5	38.36	18.26	20.11	174.34	983.24
	Mean (all)	40.01	21.94	18.07	117.43	1087.2
CSR	S.D	6	5.86	5.31	67.18	94.27
	Case 1	64.29	38.1	26.19	11827.1	10417
	Case 2	82.02	42.33	39.69	20981.4	8570.6
	Case 3	68.79	34.66	34.13	22936.9	12061
	Case 4	63.5	43.39	20.11	8724.1	12940
	Case 5	71.7	35.98	35.72	26443.2	13051
ME	Mean (all)	59.74	32.03	27.71	13430.4	12416
	S.D	9.51	7.21	7.83	8529.76	726.21
	Case 1	72.23	36.25	35.98	7023.88	56835
	Case 2	48.42	25.66	22.75	18400.9	32093
	Case 3	49.48	21.96	27.52	14619.3	23180
	Case 4	62.18	33.07	29.1	27120.8	27419
	Case 5	65.62	39.42	26.19	3201.17	25871
	Mean (all)	54.64	39.17	24.28	15194.3	28148
	S.D	8.77	11.2	8.45	8751.7	60873

$$f_5 = |\text{Low band}(\text{DWT}(I_{\text{Cyst}}(x, y)))|^2. \quad (21)$$

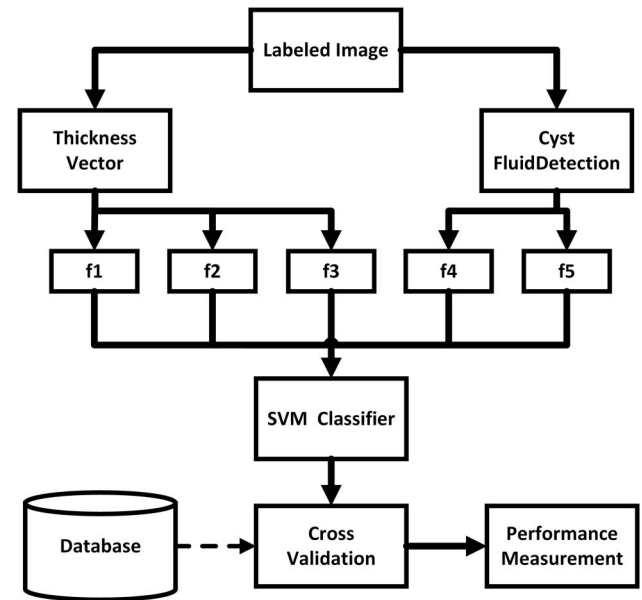
Table 2 shows the feature vectors of five randomly selected images from our local dataset. From Table 2, it can be seen that in the cases of ME and CSR, all five features deviated much more as compared to the healthy case. This is due to excessive fluid accumulation across the B-scan in the case of ME- and CSR-affected subjects.

F. Classification

1. Classifier Training

The SVM is being used in our proposed system to distinguish between ME, CSR, and healthy OCT scans. After extracting five distinct features from an OCT image, a 5D feature vector $f = \{f_1, f_2, f_3, f_4, f_5\}$ is obtained. It is then passed to the supervised classifier to make a decision based on the thickness profiles and cyst fluid present within the sub-retinal layers. SVM is among the fastest and most popular supervised classifiers [27] that have a linear hyperplane by default for classification. However, it is implemented as a nonlinear hyperplane using the multilayer perceptron kernel and Gaussian radial basis function in the proposed system. The training phase of the classifier is shown in Fig. 12.

We used a total of 30 labeled OCT images (10 ME, 10 CSR, and 10 healthy) annotated by an expert ophthalmologist to train the SVM. For each of the 30 labeled images, five distinct features are computed to form a 5D feature set ($f = \{f_1, f_2, f_3, f_4, f_5\}$). f_1, f_2 , and f_3 are based on the thickness vector $T(y)$, which is calculated by taking the absolute difference between the ILM and choroid, whereas f_4 and f_5

**Fig. 12.** Training phase of SVM.

are obtained from cyst fluid within the sub-retinal layers. After that, the feature set " f " is passed to the SVM. The performance of the SVM is measured by performing "K-fold" cross validation for different values of "K," as shown in Table 3.

2. Classification of Retinal Pathologies

Once the classifier was trained, it was used to classify unlabeled candidate images on the basis of the feature vector ($f = f(f_1, f_2, f_3, f_4, f_5)$), which is computed in the similar manner as discussed in the feature extraction section of the proposed system. We used two supervised SVMs. The first SVM classifier distinguishes between the healthy and diseased OCT scans based on four features (f_1, f_2, f_3, f_4). If the processed OCT scan is labeled as "diseased," then it is further classified as ME or CSR by the second SVM. The decision between ME and CSR is based on two features (f_4, f_5). A flowchart of the classification algorithm is shown in Fig. 13.

We have also measured the performance of our proposed system on the local (AFIO) dataset by computing sensitivity, specificity, and accuracy using Eqs. (22)–(24):

$$\text{Accuracy} = \frac{\text{TP} + \text{TN}}{\text{TP} + \text{TN} + \text{FP} + \text{FN}}, \quad (22)$$

$$\text{Sensitivity} = \frac{\text{TP}}{\text{TP} + \text{FN}}, \quad (23)$$

Table 3. Classifier Cross-Validation Performance

K	Max Accuracy
2	94.2%
4	95.7%
8	96.8%
10	98%
12	97.4%

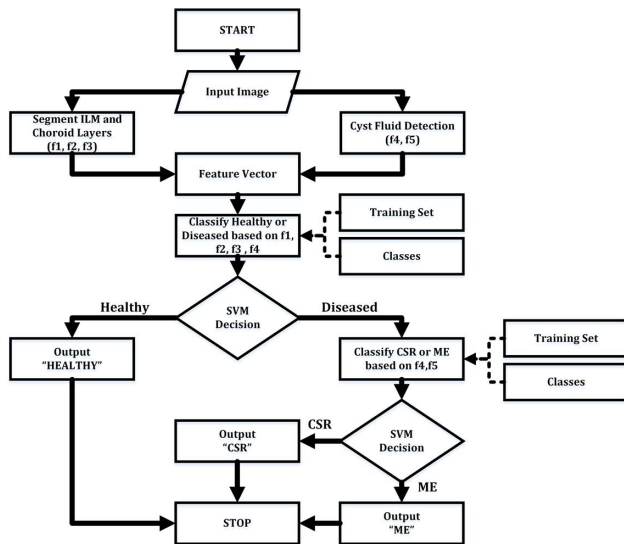


Fig. 13. Flowchart of classification algorithm.

Table 4. Results Achieved

Type	Correctly Classified	Accuracy	Sensitivity	Specificity
Healthy	28/30	97.77%	100%	93.33%
CSR	30/30			
ME	30/30			

$$\text{Specificity} = \frac{\text{TN}}{\text{TN} + \text{FP}}, \quad (24)$$

where “TP” is true positive, “TN” is true negative, “FP” is false positive, and “FN” is false negative.

3. RESULTS

We have applied the proposed algorithm to our local dataset acquired from the AFIO in Rawalpindi. All images are acquired using TOPCON’s 3D OCT-1000 camera. The dataset contains 90 OCT images, out of which 30 are of ME-affected eyes, 30 are of CSR-affected eyes, and 30 are of healthy eyes. The proposed system correctly classified 88/90 subjects, which were also confirmed by an expert ophthalmologist. Table 4 shows the results obtained for all three cases.

Apart from this, Fig. 14 shows some of the randomly selected unlabeled OCT images of all three cases that are correctly classified by our proposed system. The segmented ILM and choroid are shown in red and purple, respectively, whereas the cyst fluid is indicated by cyan.

We have also compared the performance of the SVM with other known supervised classifiers that were used in the literature. The comparison is shown in Table 5.

4. DISCUSSION

We proposed a fully automated algorithm to distinguish between three retinal pathologies using OCT images on the basis of a 5D feature vector of the candidate image. The proposed method is very robust and insensitive to speckle noise.

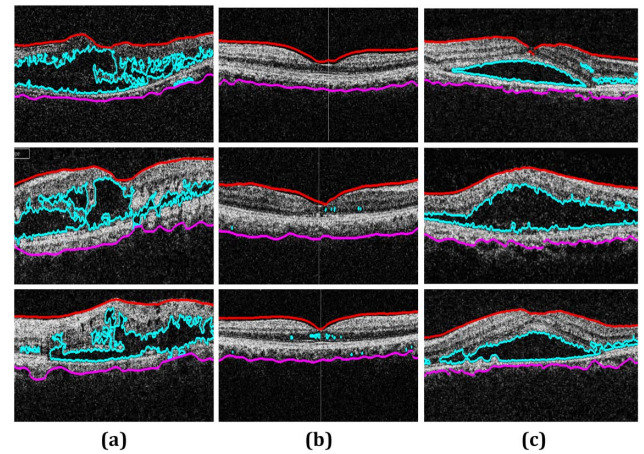


Fig. 14. Unlabeled dataset: (a) classified as ME, (b) classified as healthy, and (c) classified as CSR.

Table 5. Classifier Performance Comparison

Authors	Diseases	Dataset	Accuracy	Sensitivity	Specificity
Proposed	3	90	97.77%	100%	93.33%
[15]	2	16	—	91%	96%
[16]	3	16	87.5%	—	—
[17]	2	550	84%	93	80
[18]	3	45	95.5	100	93.75

Although we also extracted sub-retinal layers, as shown in Fig. 15, rather than relying on the correct segmentation of sub-retinal layers in extreme CSR cases, the proposed method is based on analyzing the thickness variation and cyst fluid within a B-scan of the candidate image.

Our proposed algorithm is based on five distinct features to classify three different sub-retinal pathologies. Features f_1 , f_2 , and f_3 are based on the sub-retinal thickness profiles, while f_4 and f_5 are based on sub-retinal cysts. We have computed f_1 , f_2 , and f_3 because they can give a good variation of sub-retinal thickness in healthy and CSR and ME scans. Also, healthy OCT scans do not have cyst spaces as compared to CSR and ME scans; this explains why we have a significant difference in f_4 between healthy and CSR and ME scans. f_1 , f_2 , and f_3 support f_4 . However, f_1 , f_2 , f_3 , and f_4 alone are not enough to discriminate between ME and CSR scans, as shown in Table 2. So in order to make the discrimination, we have computed the cyst energy f_5 because ME cysts contain more energy as compared to CSR cysts “ f_5 ,” as shown in Fig. 11 and also in Table 2. We have tested our algorithm on different candidate images from our local dataset that we obtained from the AFIO. Previously, we also tested our proposed algorithm on a Duke Dataset in [28] to classify ME and healthy cases, but unfortunately, we could not find any online dataset for CSR. The proposed method is quite fast and accurate in detecting small thickness variations and cyst fluid bubbles within sub-retinal layers. The approximate average time for classification is 8 s using a core i7 (1.8 GHz) fourth-generation laptop with 8 GB RAM. Moreover, our algorithm does not depend on the

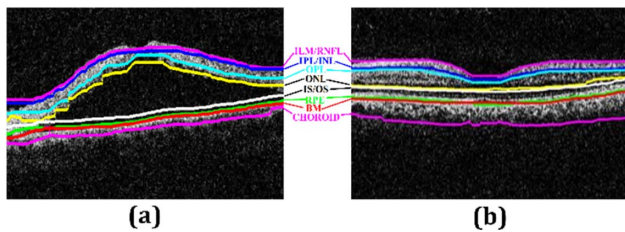


Fig. 15. Automated segmentation of sub-retinal and choroidal layers. (a) CSR-affected eye, (b) healthy eye: BM, Bruch's membrane; RPE, retinal pigment epithelium; OS, outer segment; IS, inner segment; ONL, outer nuclear layer; OPL, outer plexiform layer; IPL, inner plexiform layer; INL, inner nuclear layer; RNFL, retinal nerve fiber layer; ILM, inner limiting membrane.

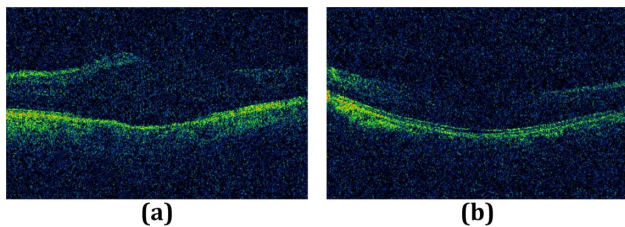


Fig. 16. Poor-quality OCT scans. (a) ILM layer not clearly visible on right side of CSR-affected OCT scan. (b) ILM layer not clearly visible in the center of a healthy OCT scan.

retinal curvature and is also rotation invariant. We have also tuned our proposed system to correctly classify all the CSR and ME subjects while compromising a bit on healthy subjects. Apart from this, there were also some noisy images in our local dataset, as shown in Fig. 16.

The proposed technique can act as an aid to an ophthalmologist. A machine can automatically segment out layers, and doctors can use the numbers to back their diagnosis. Usually, a diagnosis is subjective; such hard, quantitative facts can help standardize treatment methodologies worldwide.

Different retinal pathologies have different symptoms in OCT scans. In the future, this work can be extended for the automated detection of other retinal pathologies in a similar way by extracting some more distinct features. It can also be used for grading of ME into clinically significant macular edema (CSME) and non-CSME and grading of CSR into Type 1 and Type 2 CSR.

5. CONCLUSION

A fully automated method for the classification of macular edema, central serous retinopathy, and healthy OCT images has been proposed. Our algorithm relies on the ILM and choroid, extracted from the highly coherent 2D tensor of the candidate image. An SVM supervised classifier is used for classification. We tested our proposed system on the local dataset acquired from the AFIO. There were a total of 90 OCT images, out of which 60 were ME and CSR patients and 30 were healthy persons. Our algorithm correctly classified 88 out of 90 subjects.

Moreover, our algorithm is quite fast and achieved acceptable classifier ratings. In the future, this work can be extended for classifying other retinal diseases such as, tractional retinal detachment, MH, PEDs, and choroidal neovascularization. Our proposed algorithm can also be extended for the grading of these retinal diseases. It can also be used to detect ocular disorders such as glaucoma by measuring the thickness level between the ILM and RPE from circular optic nerve head scans.

Acknowledgment. This research was supported by the Armed Forces Institute of Ophthalmology in Rawalpindi, Pakistan, as they provided us with the dataset containing macular OCT scans of healthy persons and CSR-affected patients. We are also grateful to Dr. Zahid ul Hassan (Department of Pharmacology, Yusra Medical College, Islamabad, Pakistan) and Dr. Anjum Imdad (Department of Ophthalmology, Islamabad Medical & Dental College, Islamabad, Pakistan) for their assistance in annotating the dataset.

REFERENCES

1. Z. H. Awan, P. S. Mahar, and M. S. Memon, "Blindness and poverty," *Pakistan J. Ophthalmol.* **27**, 165–170 (2011).
2. A. Khan, Q. Riaz, F. Soomro, U. Qidwai, and U. Qazi, "Frequency and patterns of eye diseases in retina clinic of a tertiary care hospital in Karachi," *Pakistan J. Ophthalmol.* **27**, 155–159 (2011).
3. F. E. Hirai, M. D. Knudtson, B. E. K. Klein, and R. Klein, "Clinically significant macular edema and survival in type 1 and type 2 diabetes," *Am. J. Ophthalmol.* **145**, 700–706 (2008).
4. Y. J. S. Latha, C. Madhavi, and M. A. Kumar, "Visual outcome of central serous retinopathy," *Int. J. Res. Med. Sci.* **3**, 1885–1888 (2015).
5. B. Nicholson, J. Noble, F. Forooghian, and C. Meyerle, "Central serous chorioretinopathy: update on pathophysiology and treatment," *Surv. Ophthalmol.* **58**, 103–126 (2013).
6. T. Hassan, M. U. Akram, B. Hassan, A. Nasim, and S. A. Bazaz, "Review of OCT and fundus images for detecting macular edema," in *IEEE 12th International Conference on Imaging Systems*, Macau, China, September 2015.
7. P. J. Saine, "Focusing the fundus camera: a clinical approach," *J. Ophthalmic Photography* **14**, 7–24 (1992).
8. R. Z. Hannouche and M. P. Ávila, "Detection of diabetic foveal edema with bio microscopy, fluorescein angiography and optical coherence tomography," *Arquivos Brasileiros de Oftalmologia* **71**, 759–763 (2008).
9. A. Shrestha, N. Maharjan, A. Shrestha, R. Thapa, and G. Poudyal, "Optical coherence tomographic assessment of macular thickness and morphological patterns in diabetic macular edema: prognosis after modified grid photocoagulation," *Nepal J. Ophthalmol.* **4**, 128–133 (2012).
10. W. Zhang, K. Yamamoto, and S. Hori, "Optical coherence tomography for assessment of diabetic macular edema," *Int. J. Ophthalmol.* **1**, 370–373 (2008).
11. D. Ferrara, K. J. Mohler, N. Waheed, M. Adhi, J. J. Liu, I. Grulkowski, M. F. Kraus, C. Bauman, J. Hornegger, J. G. Fujimoto, and J. S. Duker, "En face enhanced-depth swept-source optical coherence tomography features of chronic central serous chorioretinopathy," *Am. Acad. Ophthalmol.* **121**, 719–726 (2014).
12. J. S. Wani, P. A. Bhat, A. Ahangar, and S. Ismail, "Role of optical coherence tomography in central serous chorioretinopathy," *J. Evol. Med. Dent. Sci.* **4**, 7801–7809 (2015).
13. M. Y. Teke, U. Elgin, P. N. Yuksekkaya, E. Sen, P. Ozdal, and F. Ozturk, "Comparison of autofluorescence and optical coherence tomography findings in acute and chronic central serous chorioretinopathy," *Int. J. Ophthalmol.* **7**, 350–354 (2014).
14. L. Zhang, W. Zhu, F. Shi, H. Chen, and X. Chen, "Automated segmentation of intraretinal cystoid macular edema for retinal 3D OCT images with macular hole," in *IEEE 12th International Symposium on Biomedical Imaging (IEEE, 2015)*, Vol. **12**, pp. 1494–1497.

15. G. R. Wilkins, O. M. Houghton, and A. L. Oldenburg, "Automated segmentation of intraretinal cystoid fluid in optical coherence tomography," *IEEE Trans. Biomed. Eng.* **59**, 1109–1114 (2012).
16. J. Sugmk, S. Kiattisin, and A. L. Lasantitham, "Automated classification between age-related macular degeneration and diabetic macular edema in OCT image using image segmentation," in *7th International Conference on Biomedical Engineering* (IEEE, 2014), pp. 1–4.
17. S. Sahar, S. Ayaz, M. U. Akram, and I. Basit, "A case study approach: iterative prototyping model based detection of macular edema in retinal OCT images," in *International Conference on Software Engineering & Knowledge Engineering* (Knowledge Systems Institute, 2015).
18. P. P. Srinivasan, L. A. Kim, P. S. Mettu, S. W. Cousins, G. M. Comer, J. A. Izatt, and S. Farsiu, "Fully automated detection of diabetic macular edema and dry age-related macular degeneration from optical coherence tomography images," *Biomed. Opt. Express* **5**, 3568–3577 (2014).
19. S. Y. Lee, P. F. Stetson, H. Ruiz-Garcia, F. M. Heussen, and S. R. Sadda, "Automated characterization of pigment epithelial detachment by optical coherence tomography," *Invest. Ophthalmol. Visual Sci.* **53**, 164–170 (2012).
20. D. Cabrera Fernández, H. M. Salinas, and C. A. Puliafito, "Automated detection of retinal layer structures on optical coherence tomography images," *Opt. Express* **13**, 10200–10216 (2005).
21. D. Cabrera Fernández and H. M. Salinas, "Extracting subretinal layers on stratus OCT images via a structure tensor approach combined with a nonlinear diffusion process," *Invest. Ophthalmol. Visual Sci.* **46** (2005).
22. J. Bigun and G. Granlund, "Optimal orientation detection of linear symmetry," Technical Report LiTH-ISY-I-0828 (Linköping University, 1986).
23. J. S. Lim, "Image restoration," in *Two-Dimensional Signal and Image Processing* (Prentice-Hall, 1990), pp. 536–540.
24. H. Knutsson, "Representing local structure using tensors," in *Proceedings of 6th Scandinavian Conference on Image Analysis* (Oulu University, 1989), pp. 244–251.
25. M. Sezgin and B. Sankur, "Survey over image thresholding techniques and quantitative performance evaluation," *J. Electron. Imaging* **13**, 146–165 (2004).
26. J. Canny, "A computational approach to edge detection," *IEEE Trans. Pattern Anal. Mach. Intell.* **PAMI-8**, 679–698 (1986).
27. R. E. Fan, K. W. Chang, C. J. Hsieh, X. R. Wang, and C. J. Lin, "LIBLINEAR: a library for large linear classification," *J. Mach. Learn. Res.* **9**, 1871–1874 (2008).
28. T. Hassan, M. U. Akram, B. Hassan, A. M. Syed, and S. A. Bazaz, "Automated segmentation of subretinal layers for the detection of macular edema," *Appl. Opt.* **55**, 454–461 (2016).